A New $La_{2/3}Li_xTi_{1-x}Al_xO_3$ Solid Solution: Structure, Microstructure, and Li^+ Conductivity

Ainhoa Morata-Orrantia, Susana García-Martín,* Emilio Morán, and Miguel Ángel Alario-Franco

Departamento de Química Inorgánica, Facultad de Ciencias Químicas, Universidad Complutense, 28040 Madrid, Spain, EU

Received June 22, 2001. Revised Manuscript Received April 3, 2002

The stoichiometry range, crystal chemistry, ionic conductivity, and electrochemical window of the $La_{2/3}Li_xTi_{1-x}Al_xO_3$ system with perovskite-related structure have been studied. The range of the existence of the solid solution is ($0.06 = x = 0.3$). Powder X-ray diffraction and transmission electron microscopy results show that these oxides have a unit cell multiple of the perovskite cell with dimensions $a \approx \sqrt{2}a_p$, $b \approx \sqrt{2}a_p$, $c \approx 2a_p$. The ionic conductivity of the materials and its dependence on composition and temperature have been examined by complex impedance spectroscopy. Lithium ion conductivity increases with increasing lithium content up to a value (7.6×10^{-5} S cm^{-1} at room temperature) corresponding to $x = 0.25$. Electrochemical experiments indicate that these materials can be used as solid electrolytes in secondary batteries having Li metal as the anode down to 1.6 V.

Introduction

Materials with perovskite-related structure are attractive candidates for a great variety of applications. The compounds of general formula $La_{2/3-x}Li_{3x}TiO_3$ ($0.036 < x < 0.14$) have the highest Li^+ conductivity reported in the literature to date,[1−4] being potentially good electrolytes for solid-state lithium secondary batteries. However, together with the high bulk conductivity ($\sigma_{bulk} \approx 1 \times 10^{-3}$ S cm^{-1} at room temperature), large grain boundary resistances are observed in these materials. Besides, their electrochemical intercalation properties[5,6] lead to the reduction of Ti^{4+} to Ti^{3+} at relatively low potentials (≈2 V) when using Li metal as the anode, with the appearance of electronic conductivity and the short-circuiting of the cell. These facts clearly limit the use of these oxides as solid electrolytes. Therefore, attention to ceramic processing is required to optimize the overall sample conductivities. Moreover, reduction of the materials, (i.e., electronic conductivity) must be avoided while the high ionic conductivity is maintained.

A great amount of research has focused on the Ti cation substitution in the $La_{2/3-x}Li_{3x}TiO_3$ system by other metal ions with less tendency toward reduction against Li metal. In this way, $La_{0.67}Li_{0.1}Mg_{1/2}W_{1/2}O_3$ has been prepared,[7] but the ionic conductivity of this material is lower than the conductivity of the titanates and reaction with lithium is still observed. An increase of the Li^+ conductivity with the substitution of the Ti by Ge has however been reported in the $(La_{0.5}Li_{0.5})Ti_{1-x}Ge_xO_3$ system[8] and attributed to the lower atomic size of the Ge relative to Ti, but electrochemical experiments were not performed. The $La_{1/3-x}Li_{3x}NbO_3$ ($0 \le x \le 0.06$) solid solution with a perovskite-related structure has also been studied.[9−10] These niobates have a lower Li^+ conductivity than the titanates but the grain boundary contributions to the overall electrical resistance are negligible; however, niobium reduction is observed below 1.75 V against a Li metal anode. The ionic conductivity of the $La_{1/3-x}Li_{3x}TaO_3$ ($0 \le x \le 0.16$) materials has recently been analyzed[11,12] but again their electrochemical behavior has not been studied.

We present in this paper a study of the simultaneous lithium addition and titanium substitution by aluminum in the system $La_{2/3}Li_xTi_{1-x}Al_xO_3$. Trivalent aluminum is not easily reducible, and if the substitution is high enough, we could prevent the reaction against Li metal. Besides, in line with previous work on Ti replacement by Ge,[8] the ionic conductivity of the materials could increase with this substitution because of the lower effective ionic radii of Al^{3+} (r_{VI} $Al^{3+} = 0.53$ Å) compared to that of Ti^{4+} (r_{VI} $Ti^{4+} = 0.605$ Å). We report in here the stoichiometry range, crystal chemistry, electrical properties, and electrochemical window versus Li of the $La_{2/3}Li_xTi_{1-x}Al_xO_3$ solid solution.

* To whom correspondence should be addressed: Tel.: 91-394214. Fax: 91-3944352. E-mail: sgmartin@quim.ucm.es.

(1) Inaguma, Y.; Liquan, C.; Itoh, M.; Nakamura, T.; Uchida, T.; Ikuto, H.; *Solid State Commun.* **1993**, *86*, 689.
(2) Kawai, H.; Kuwano, J. *J. Electrochem. Soc.* **1994**, *141*, L78.
(3) Inaguma, Y.; Itoh, M. *Solid State Ionics* **1996**, *86*−*88*, 257.
(4) Harada, Y.; Ishigaki, T.; Kawai, M.; Kuwano, J. *Solid State Ionics* **1998**, *108*,407.
(5) Shan, Y. J.; Chem, L.; Inaguma, Y.; Itoh, M.; Nakamura, T. *J. Power Sources* **1995**, *54*,397.
(6) Bohnke, O.; Bohnke, C.; Fourquet, J. L. *Solid State Ionics* **1996**, *91*, 21.
(7) Inaguma, Y.; Chem, L.; Itoh, M.; Nakamura, T. *Solid State Ionics* **1994**, *70/71* 196.
(8) Chung, H. T.; Kim, J. G.; Kim, M. G. *Solid State Ionics* **1998**, *107*, 153.
(9) Kawakami, Y.; Ikuta, H.; Wakihara, M. *J. Solid State Electrochem.* **1998**, *2*, 206.
(10) García-Martín, S.; Rojo, J. M.; Tsukamoto, M.; Morán, E.; Alario-Franco, M. Á. *Solid State Ionics* **1999**, *116*, 11.
(11) Mizumoto, K.; Hayashi, S. *Solid State Ionics* **1996**, *116*, 263.
(12) Mizumoto, K.; Hayashi, S. *Solid State Ionics* **2000**, *127*, 241.

10.1021/cm011149s CCC: $22.00
Published on Web 06/04/2002

Experimental Section

Different compositions of the $La_{2/3}Li_xAl_xTi_{1-x}O_3$ system were prepared from stoichiometric amounts of Li_2CO_3 (Merck 99%), La_2O_3 (Aldrich 99.999%), TiO_2 (Aldrich 99.99%), and Al_2O_3 (Aldrich 99.99%). La_2O_3 was heated overnight at 1000 °C and TiO_2 and Al_2O_3 at 700 °C prior to weighing. The mixtures were ground and then heated in Pt boats for 6 h for decarbonation. Afterward, the samples were reground, pelleted, covered with powder of the sample of the same composition to prevent lithia loss, and fired at 1100 °C for 12 h followed by further grinding, repelleting, and refiring at 1300 °C for another 12 h. To study the evolution of the crystal structure with temperature, small amounts of sample were wrapped in Pt foil envelopes, annealed isothermally at different temperatures, and quenched to room temperature on a brass plate.

The molar ratio of the metals in the compounds was determined by inductively coupled plasma (ICP) spectroscopy using a JY-70 plus instrument. To perform the ICP analysis, a solution protocol was optimized. Samples were treated with a mixture of nitric, hydrochloric, and hydrofluric acids in a 3:2:1 molar ratio at 150 °C in a high-pressure Teflon reactor fitted with a temperature sensor and placed inside of a MILESTONE microwave digestion furnace (ASM-1200 model).

Crystalline phase identification and determination of the lattice parameters were carried out by powder X-ray diffraction (XRD) using a Philips X'PERT diffractometer with Cu $K\alpha_1$ radiation, a curved Cu monochromator, and the Philips X'PERT PEAPD software. The patterns were taken at step mode with a step size equal to 0.02° (2θ) and time per step equal to 10 s.

The microstructure of the materials was characterized by selected area electron diffraction (SAED) and transmission electron microscopy (TEM). Samples were ground in *n*-butyl alcohol and ultrasonically dispersed and drops of the resulting suspension were deposited in carbon-coated grids. SAED studies were performed with an electron microscope, JEOL 2000 FX (double tilt ±45 °), working at 200 kV and TEM studies with an electron microscope, Philips CM 200 FEG, working at 200 kV.

Impedance measurements were performed in an impedance/gain phase analyzer Solartron 1255A with dielectric interface 1296. Pellets of about 13-mm diameter and 2-mm thickness were prepared by pressing the powder samples and sintering at 1300 °C. Electrodes were made by coating opposite pellet faces with platinum paste and heating to 850 °C. Measurements were carried out in air on a heating cycle from room temperature to 100 °C and in a frequency range $1 \times 10^{-3} - 6 \times 10^6$ Hz.

The electrochemical window of the materials was examined by potentiostatic and galvanostatic discharge and charge using Swagelok cells and a multichannel potentiostatic/galvanostatic MacPile system.[13] Li foil was used as the counter electrode and 1 M solution of $LiPF_6$ in ethylene carbonate (EC) and dimethylene carbonate (DMC) as the electrolyte. The working electrode was a mixture of the samples, carbon black and binder at the ratio 87:8.7:4.3 (in wt %). Cells were assembled in an argon-filled glovebox. Cyclic voltametries were carried out within the potential range 0−3 V vs Li/Li^+ at the scanning rate of 20 mV/2 h. Cells were galvanostatically discharged and charged using a current density of 30 $\mu A/cm^2$ between 3 and 1 V.

Results and Discussion

Stoichiometric Range and Crystal Chemistry of the Solid Solution $La_{2/3}Li_xTi_{1-x}Al_xO_3$. Single-phase materials are found over the composition range $0.06 \leq x \leq 0.3$. Table 1 shows the chemical composition analysis data of three samples corresponding to different x values. Owing to the good agreement between analytical and nominal values, nominal compositions will be kept during the discussion.

Table 1. Analysis Data for Three Samples of $La_{2/3}Li_xTi_{1-x}Al_xO_3$

x	nominal composition	experimental composition
0.1	$La_{0.67}Li_{0.1}Ti_{0.9}Al_{0.1}O_3$	$La_{0.68}Li_{0.09}Ti_{0.87}Al_{0.10}O_3$
0.2	$La_{0.67}Li_{0.2}Ti_{0.8}Al_{0.2}O_3$	$La_{0.72}Li_{0.18}Ti_{0.81}Al_{0.20}O_3$
0.3	$La_{0.67}Li_{0.3}Ti_{0.7}Al_{0.3}O_3$	$La_{0.68}Li_{0.27}Ti_{0.67}Al_{0.27}O_3$

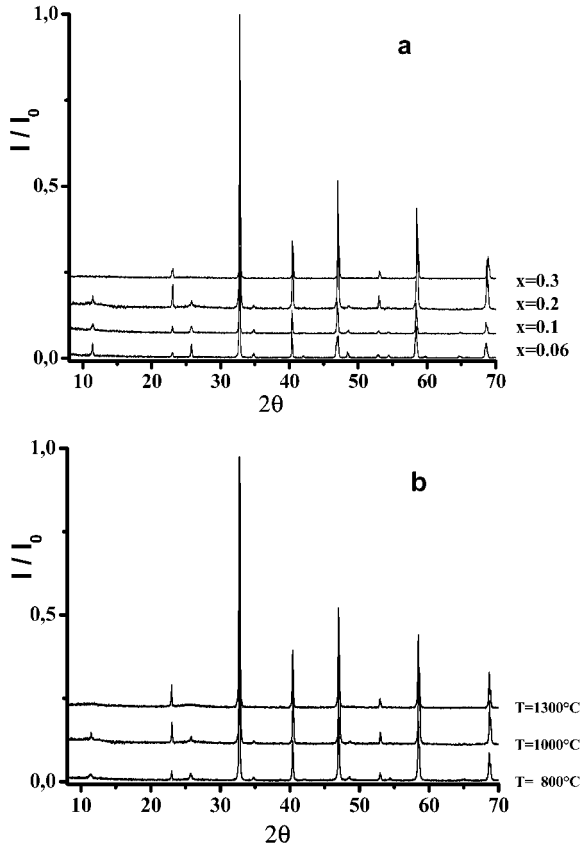

Figure 1. Powder XRD patterns of (a) $La_{2/3}Li_xTi_{1-x}Al_xO_3$ (x = 0.06, 0.1, 0.2, and 0.3) annealed at 1000 °C and (b) $La_{2/3}Li_xTi_{1-x}Al_xO_3$ (x = 0.2) annealed at 800, 1000, and 1300 °C.

The powder X-ray diffraction patterns of these materials are characteristic of a perovskite-related structure but modifications of the patterns with both the composition and the annealing temperature of the samples are observed, as also happens in the $La_{0.5+x}Li_{0.5-x}TiO_3$ ($0.025 < x < 0.13$) solid solution.[14] Figure 1a shows the powder XRD patterns of four samples with different compositions annealed at 1000 °C and quenched from this temperature. Superlattice reflections with respect to the ideal cubic perovskite structure are observed in the patterns with $0.06 \leq x \leq 0.2$. These extra reflections double the c_p lattice parameter ("p" refers to the cubic perovskite unit cell. Strictly speaking, perovskites are characterized by a_p and cubic crystals do not need c_p; however, it is convenient to choose the direction of doubling of the structure) and their intensity decreases when x increases in such a way that they are almost invisible in the sample corresponding to $x = 0.3$. Figure 1b shows the powder XRD

(13) Mouget, C.; Chabre, Y. *Multichannel Potentistatic and Galvanostatic System MacPile*, Licensed by CNRS and UJF Grenoble to Bio-login Corp., 1 avenue de l'Europe, F-38640 Claix, 1991.

(14) Robertson, A. D.; García-Martín, S.; Coats, A.; West, A. R. *J. Mater. Chem.* **1995**, *5* (9), 1405.

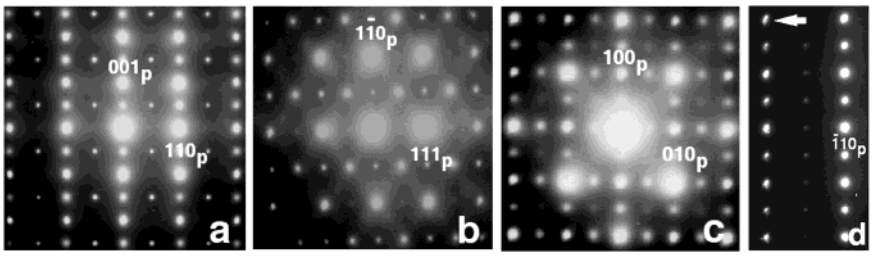

Figure 2. SAED patterns of $La_{2/3}Li_xTi_{1-x}Al_xO_3$ ($x = 0.2$) annealed at 1300 °C along the $[\bar{1}10]_p$ (a), $[\bar{1}\bar{1}2]_p$ (b), and $[001]_p$ (c) zone axes and an enlarged view of part of the pattern along the $[\bar{1}10]_p$ zone axes to show the spot splitting (d).

patterns of the oxide of composition corresponding to $x = 0.2$ annealed at different temperatures. We can see that the intensity of the superlattice reflections decreases when the annealing temperature increases.

However, despite the differences observed by XRD, all the materials have the same basic unit cell, as seen by electron diffraction and microscopy, and described in what follows.

Figure 2 shows three SAED patterns of different zone axis of the oxide of composition corresponding to $x = 0.2$ annealed at 1300 °C. The strongest spots in these patterns have been indexed according to the ideal perovskite cell. The XRD pattern of this material can be considered as characteristic of the ideal perovskite structure (Figure 1b). Nevertheless, $(0\ 0\ {}^1/_2)_p$ superlattice reflections which double the *c*-axis are observed in the pattern of the $[\bar{1}10]_p$ zone axis. Besides, $({}^h/_2\ k/_2\ {}^1/_2)_p$ are also seen in the patterns of the $[\bar{1}10]_p$ and $[\bar{1}\bar{1}2]_p$ zone axes. All these intensity maxima make us consider a true unit cell of dimensions $\approx\sqrt{2}a_p \times \approx\sqrt{2}a_p \times \approx 2a_p$. However, in the pattern corresponding to the $[001]_p$ zone axis, $({}^h/_2\ 0\ 0)_p$ and $(0\ {}^k/_2\ 0)$ reflections, which apparently double the other two lattice parameters, also do appear. Therefore, either the cell is $\approx 2a_p \times \approx 2a_p \times \approx 2a_p$ or the crystal is formed by domains of the $\approx\sqrt{2}a_p \times \approx\sqrt{2}a_p \times \approx 2a_p$ cell in which the long *c*-axis is randomly oriented along the three different space directions. Electron microscopy can indeed clear up the ambiguity: Figure 3a shows a TEM image corresponding to the $[001]_p$ zone axis. Three different kinds of regions can be seen: regions with $\approx 2a_p$ periodicity along the $[100]_p$ direction; small areas having $\approx 2a_p$ periodicity along the $[010]_p$ direction; and areas showing $\approx\sqrt{2}a_p$ periodicity along the $[110]_p$ direction. We then conclude that the crystal is formed by three sets of microdomains of the $\approx\sqrt{2}a_p \times \approx\sqrt{2}a_p \times \approx 2a_p$ cell with the *c*-axis oriented along one of the three main crystallographic directions ($[100]_p$, $[010]_p$, and $[001]_p$) in each domain set.

The SAED patterns are similar although not identical (dimensional changes are observed) for all the materials independent of the composition or the annealing temperature, indicating that the oxides of the solid solutions $La_{2/3}Li_xTi_{1-x}Al_xO_3$ do have the so-called diagonal perovskite-related structure with lattice parameters $a \approx \sqrt{2}a_p$, $b \approx \sqrt{2}a_p$, $c \approx 2a_p$. This distortion of the perovskite structure is due to the tilting of the $(Ti,Al)O_6$ octahedra network to accommodate the small size of the Li^+ and La^{3+} ions.[15,16] Besides, Li^+, La^{3+}, and vacancies ordering could exist.

The intensity of the superlattice reflections in the XRD patterns is likely to depend on the size of the domains of the $\sqrt{2}a_p \times \sqrt{2}a_p \times 2a_p$ cell in such a way that broad (almost invisible) peaks are due to a microdomain microstructure. In fact, we have observed large domains for the samples annealed at lower temperatures. Figure 3b shows an image corresponding to the $[001]_p$ zone axis for the sample with $x = 0.2$ annealed at 1000 °C. Three different domains are seen on the picture with the *c*-axis oriented along each of the three crystallographic directions. The annealing at temperatures lower than the synthesis temperature allows the

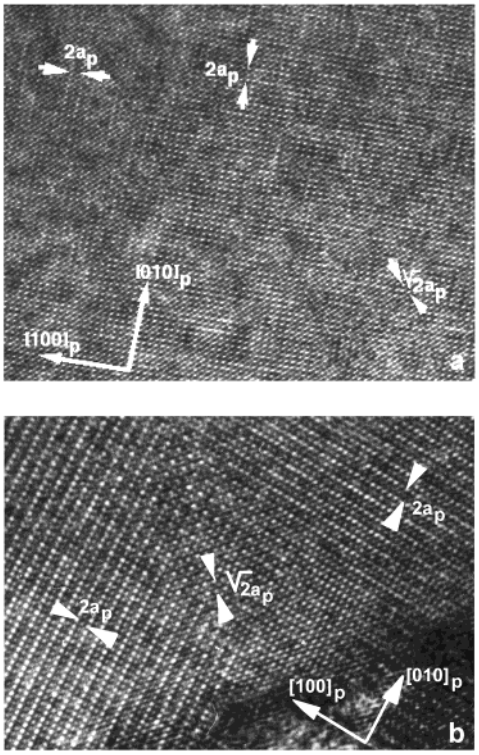

Figure 3. TEM images of $La_{2/3}Li_xTi_{1-x}Al_xO_3$ ($x = 0.2$) corresponding to the $[001]_p$ zone axis: (a) sample annealed at 1300 °C and (b) sample annealed at 1000 °C.

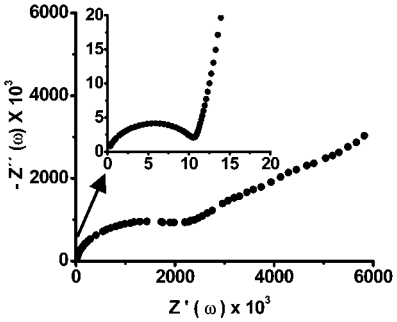

Figure 4. Complex impedance diagrams at 22 °C of $La_{2/3}Li_xTi_{1-x}Al_xO_3$ ($x = 0.15$).

(15) Thomas, N. W. *Acta Crystallogr. B* **1996**, *52*, 16.
(16) Woodward, P. M. *Acta Crystallogr. B* **1997**, *53*, 44.

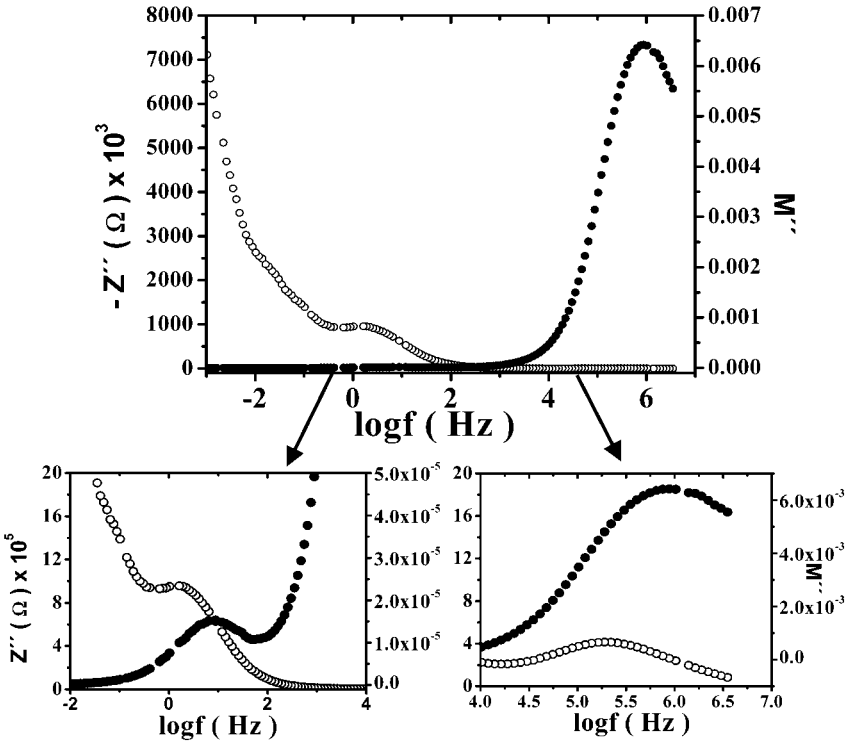

Figure 5. Imaginary impedance and imaginary modulus vs frequency at 22 °C for $La_{2/3}Li_xTi_{1-x}Al_xO_3$ ($x = 0.15$).

Table 2. Lattice Parameters of $La_{2/3}Li_xTi_{1-x}Al_xO_3$

x	a (Å)	b (Å)	c (Å)	V (Å^3)
0.06	5.479	5.471	7.772	232.98
0.1	5.478	5.469	7.761	232.51
0.15	5.469	5.466	7.729	231.11
0.2	5.465	5.463	7.729	230.77
0.25	5.457	5.454	7.717	229.68
0.3	5.454	5.450	7.715	229.12

growth of the domains. Other factors apart from the size of the domains, such as cation ordering, can indeed affect the intensity of the superlattice reflections in the XRD patterns.

Powder XRD patterns of the samples could be indexed using either the orthorhombic $\approx\sqrt{2}a_p \times \approx\sqrt{2}a_p \times \approx 2a_p$ unit cell or a tetragonal cell with lattice parameters $a = b \approx \sqrt{2}a_p$, $c \approx 2a_p$. However, splitting of the $(110)_p$ reflections into two can be seen in the SAED pattern corresponding to the $[\bar{1}10]_p$ zone axis far from the zone center (see arrow in Figure 2d). This splitting is due to the slightly different dimensions of the a and b lattice parameters and the domain formation of the crystal with different orientations of the lattice parameters. Consequently, the powder patterns of the samples have been indexed using the orthorhombic $\approx\sqrt{2}a_p \times \approx\sqrt{2}a_p \times \approx 2a_p$ cell. Table 2 shows the lattice parameters of the $La_{2/3}Li_xTi_{1-x}Al_xO_3$ ($0.06 \le x \le 0.3$) oxides annealed at 1000 °C. The lattice parameters decrease in a linear way with increasing lithium content.

Electrical Properties of the $La_{2/3}Li_xTi_{1-x}Al_xO_3$ ($0.06 \le x \le 0.3$) Oxides. The lithium ion conductivity of the materials has been studied by impedance measurements. All the compounds of the solid solution present similar electrical behavior, which we are going to comment on in the following for the sample corresponding to $x = 0.15$.

Figure 4 shows the complex impedance diagram at 22 °C. Two semicircles (depressed below the real axis) and a spike at the lowest frequencies are observed. The arc at the highest frequency is ascribed to the bulk of the material while the other arc can be attributed to grain boundary effects. The capacitances associated with the two semicircles are on the order of 10^{-11} and 10^{-8} F, which are characteristic of bulk and grain boundary effects, respectively; the capacitance associated with the spike is on the order of 10^{-7} F, which is typical of the blocking effect of the ionic charge carriers at the electrode−sample interface.[17] These effects are also distinguished in the Z" and M" vs frequency plots (Figure 5). Two peaks appear for both Z" and M": the peaks at high frequency correspond to the bulk process while those at low frequency can be attributed to the effect of the grain boundaries. The equivalent circuit, which models these results, consists of two parallel circuits (representing the behavior of the bulk of the material and the grain boundary effects) and a capacitance (representing the blocking at the electrodes). A frequency-dependent capacitance and conductance form each of the parallel circuits. The three components of the circuit are situated in series.

Bulk conductivity and grain boundary conductivity values have been extracted from the impedance complex plane diagrams at different temperatures. Figure 6 shows the plots of log σ_{bulk} vs $1000/T$ for four compositions. The data fit an Arrhenius-type equation, $\sigma = \sigma_o \exp(E_\sigma/KT)$ where E_σ is the activation energy of the process. Table 3 shows the ionic conductivity values at 300 K and the corresponding activation energies for different compositions on the solid solution. In contrast, the activation energy does not seem to depend on the composition of the oxide. The conductivity increases with increasing lithium content up to a value corre-

(17) Irvine, J. T. S.; Sinclair, D. C.; West, A. R. *Adv. Mater.* **1990**, *2* (3), 138.

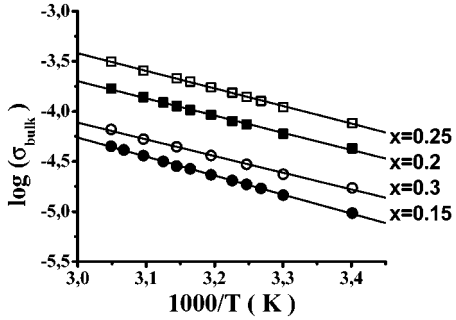

Figure 6. Plots of log σ_{bulk} vs 1000/T for $La_{2/3}Li_xTi_{1-x}Al_xO_3$ (x = 0.15, 0.2, 0.25, and 0.3).

Table 3. Bulk and Grain Boundary Conductivity Values at 300 K and Activation Energies of $La_{2/3}Li_xTi_{1-x}Al_xO_3$

x	σ_{bulk} (S cm^{-1})	σ_{gb} (S cm^{-1})	$E_{a,b}$ (eV)	$E_{a,gb}$ (eV)
0.06	1.684×10^{-6}	3.069×10^{-8}	0.36	0.41
0.1	7.336×10^{-6}	3.156×10^{-8}	0.35	0.41
0.15	9.655×10^{-6}	5.038×10^{-8}	0.36	0.39
0.2	4.28×10^{-5}	1.565×10^{-7}	0.33	0.41
0.25	7.658×10^{-5}	3.299×10^{-7}	0.35	0.41
0.3	1.718×10^{-5}	6.434×10^{-8}	0.33	0.39

sponding to x = 0.25. This behavior is characteristic of a solid solution in which the increase in the number of charge carriers enhances the conductivity up to a composition after which the conductivity decreases due to the decrease in the number of nonoccupied sites for the ions to move in. The highest bulk conductivity in the system (7.6×10^{-5} S cm^{-1} at room temperature) is still lower than the conductivity observed in the oxides of the $La_{2/3-x}Li_{3x}TiO_3$ solid solution so the hypothesis of the increase of lithium conduction with the decrease of the B cation in the ABO_3 perovskite lattice (ref 8) does not seem to apply to our system; however, it is to be recalled that the ratio of charge carriers to the number of nonoccupied positions in both solid solutions is not the same.

Electrochemical Measurements. Figure 7a shows the cyclic voltammogram and Figure 7b the voltage−composition curves for three charge and discharge cycles of a cell using the material of composition corresponding to x = 0.2 as the working electrode. Strong cathodic peaks below 1.5 V are observed in the voltammogram. The peak at 1.3 V can be attributed to the reduction of

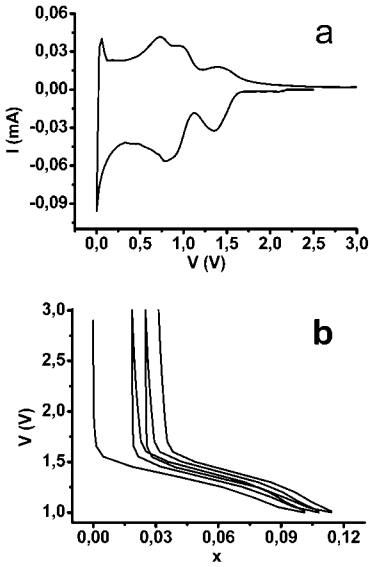

Figure 7. Cyclic voltammogram (a) and voltage−composition curves (b) for Li/1 M $LiPF_6$ (EC, DMC)/$La_{2/3}Li_xTi_{1-x}Al_xO_3$ (x = 0.2).

Ti^{4+} to Ti^{3+} because of the electrochemical Li intercalation into the material. The galvanostatic experiment shows that the material can reversibly insert up to 0.1 mol of lithium ions per formula unit from 1.6 to 1 V. The losses in capacity in the charge processes are rather small (about 12% in the first cycle and <10% in further cycles) so they are likely to be associated to the loss of electrical contact between some of the cathode particles. Similar electrochemical results are obtained for other oxides of the solid solution with different compositions. As a result of the intercalation reaction, electronic conductivity appears in the oxide and therefore it can be used as a solid electrolyte in secondary batteries down to 1.6 V having Li metal as the anode.

Acknowledgment. Authors thank CICYT (MAT 98-1053 and MAT98-0729) for financial support and the Microscopy Centre Luis Bru and the X-ray diffraction C.A.I. from U.C.M. for technical assistance.

CM011149S